



**CoxNi<sub>100-x</sub> nanoparticles encapsulated by curved graphite layers: controlled in-situ metal-catalytic preparation and broadband microwave absorption**

Journal:	<i>Nanoscale</i>
Manuscript ID:	NR-ART-06-2015-003745.R1
Article Type:	Paper
Date Submitted by the Author:	08-Aug-2015
Complete List of Authors:	<p>Ma, Song; Institute of Metal Research, Chinese Academy of Sciences, Shenyang National Laboratory for Material Science</p> <p>Wang, Han; Institute of Metal Research,CAS, Shenyang National Laboratory for Material Science</p> <p>Dai, Yingying; Institute of Metal Research,CAS, Shenyang National Laboratory for Material Science</p> <p>Geng, Dianyu; Institute of Metal Research,CAS, Shenyang National Laboratory for Material Science</p> <p>Li, Da; Institute of Metal Research,CAS, Shenyang National Laboratory for Material Science</p> <p>An, Jing; Central Iron &amp; Steel Research Institute, Division of Functional Material Research</p> <p>He, Jun; Central Iron &amp; Steel Research Institute, Division of Functional Material Research</p> <p>Liu, Wei; Institute of Metal Research,CAS, Shenyang National Laboratory for Material Science</p> <p>Zhang, Zhi-Dong; Institute of Metal Research, Chinese Academy of Sciences, Magnetism and Magnetic Materials Division</p>



# Co<sub>x</sub>Ni<sub>100-x</sub> nanoparticles encapsulated by curved graphite layers: controlled in-situ metal-catalytic preparation and broadband microwave absorption†

Received 00th January 20xx,  
Accepted 00th January 20xx

DOI: 10.1039/x0xx00000x

www.rsc.org/

H. Wang,<sup>a\*</sup> Y. Y. Dai,<sup>a</sup> D. Y. Geng,<sup>a</sup> S. Ma,<sup>a\*</sup> D. Li,<sup>a</sup> J. An,<sup>b</sup> J. He,<sup>b</sup> W. Liu,<sup>a</sup> Z. D. Zhang<sup>a</sup>

We report a one-step approach of preparing dispersive Co<sub>x</sub>Ni<sub>100-x</sub> nanoparticles completely encapsulated by curved graphite layers. The nanoparticles were prepared by evaporating Co-Ni alloys and the shell of graphite layers was formed by in-situ metal-catalytic growth on the surface of nanoparticles whose layer number was controlled by tuning the Co content of the alloys. By modulating the composition of magnetic core and the layer number of shell, the magnetic and dielectric properties of these core/shell structures are simultaneously optimized and their permeability and permittivity were improved to obtain the enhanced electromagnetic match. As a result, the bandwidth of reflection loss (RL) exceeding -20 dB (99 % absorption) of the nanocapsules is 9.6 GHz for S1, 12.8 GHz for S2, 13.5 GHz for S3 and 14.2 GHz for S4. The optimal RL value reaches -53 dB at 13.2 GHz for an absorber thickness of 2.55 mm. An optimized impedance match by controlling growth of core and shell is responsible for this extraordinary microwave absorption.

## Introduction

The design and synthesis of electromagnetic-wave (EMW) absorbing materials for civilian and military applications have become a cutting-edge subject due to serious electromagnetic (EM) problems, such as EM radiation/pollution, EM leakage, EM interference and compatibility.<sup>1-6</sup> Soft-magnetic metallic nanomaterials (especially Co, Ni and their alloys) as new-type EMW absorbers in the gigahertz frequency range are expected to replace the traditional ferrite materials which possess high absorption only in the mega Hertz frequency range due to Snoek's limit.<sup>3,4,6-9</sup> The application of metallic nanoparticles in practical microwave absorption is impeded because of easy agglomeration, oxidization, corrosion and EM mismatch.<sup>10-12</sup>

The magnetic-core/dielectric-shell structure has been proved to be efficient in improving thermal, electrical, optical, magnetic, electromagnetic and chemical performances of materials.<sup>10,12,13</sup> Compared with oxides (SiO<sub>2</sub>, ZnO and Al<sub>2</sub>O<sub>3</sub>) and conducting polymers, carbon can be considered as ideal

shell material for EMW absorption, because of its low price, lightweight, high stability and protection of the magnetic cores against environment corrosion.<sup>14-16</sup> Various carbon-based materials and magnetic nanoparticles have been combined by wet chemical method or mechanical mixing to improve the EMW absorption, such as magnetic nanoparticle/carbon fiber composites,<sup>17</sup> magnetic nanoparticle/carbon nanotubes composites,<sup>15,16,18</sup> magnetic nanoparticle/graphene composites,<sup>19,20</sup> magnetic nanoparticle/carbon monolith.<sup>11</sup> However, in these nanocomposites, the concentration of magnetic nanoparticles is low and the nanoparticles may be easily destroyed by high pressure or by moist air. Another key point for enhancing the absorption ability of the magnetic/dielectric type of core/shell structure is its possibility for the appropriate EM match between core and shell. Based on previous researches, the core/shell structure with magnetic transition metal core and curved graphite shell has shown extraordinary EMW absorption with good EM match.<sup>4,10,14,16,21</sup> However, how to explore optimal EM match in these core/shell structures becomes an urgent issue in EMW absorption materials research. Because the EM match is determined by the magnetic and dielectric behaviour of core and shell, the composition of magnetic core and the shell thickness of graphite shell turn into crucial parameters for developing this novel and controllable core/shell structures which have simultaneously tunable magnetic properties and dielectric properties for solving EM problems.

<sup>a</sup> Shenyang National Laboratory for Materials Science, Institute of Metal Research, Chinese Academy of Sciences, 72 Wenhua Road, Shenyang, 110016, P. R. China.

<sup>b</sup> Division of Functional Material Research, Central Iron & Steel Research Institute, Beijing, 100081, P. R. China.

† Electronic Supplementary Information (ESI) available: two figures are included for illustrating the size distribution and electromagnetic loss factor of the prepared nanocapsules. DOI: 10.1039/x0xx00000x

\* Corresponding author: [songma@imr.ac.cn](mailto:songma@imr.ac.cn), [wanghan838@gmail.com](mailto:wanghan838@gmail.com)

High-temperature arc-plasma evaporation has been shown to be a powerful technique for preparing core/shell structures.<sup>4, 10, 14, 22</sup> Among ferromagnetic transition metals (Fe, Co, Ni), Fe has the largest atomic moment of  $2.2 \mu_B$ , but Fe easily acts with C to form iron carbides to decrease the quality of magnetic core, which increases complexity for analysis of microwave absorption mechanism.<sup>23, 24</sup> For Co and Ni, they difficultly react with C,<sup>25</sup> moreover the solubility of C in Co and Ni is very low, which lead that C atoms easily migrate from the interior of Co or Ni nanoparticle to the surface to form graphite shell during preparation of Co or Ni nanoparticles in arc-plasma evaporation process.<sup>26, 27</sup> With another important fact that Co and Ni are always taken for preparing high quality graphene, Co and Ni nanoparticles could take this predominance as the catalyst for growth of graphite shell. When CoNi nanoparticles are chosen as core for the purpose of controlling their magnetic properties, they also can be used for in-situ tuning the growth of graphite shell simultaneously, therefore, the CoNi/C functions an excellent and novel module system to study the roles of C shell and CoNi magnetic core on microwave absorption. The composition of the nanoparticles has crucial influence not only on their magnetic properties but also on the diffusion of carbon atoms within the cores and the catalytic growth of the carbon shell. For example, at 1000 °C, the diffusion coefficients of carbon in nickel and cobalt are about  $10^{-7} \text{cm}^2/\text{s}$  and  $4 \times 10^{-7} \text{cm}^2/\text{s}$ , respectively, the difference being due to the larger size of cobalt atom.<sup>28, 29</sup> The catalytic growth of the carbon atoms on Co-Ni binary alloys is larger than on pure Ni and Co.<sup>30, 31</sup> Therefore, we expect that tuning the Co content in Co-Ni alloys may be an effective approach to control the growth of graphite layers. This will extraordinarily improve the EMW absorption because, as we have shown previous work, by adjusting the thickness of shell the impedance match can be optimized.<sup>10</sup>

In this paper, we report one-step synthesis of  $\text{Co}_x\text{Ni}_{100-x}$  nanoparticles, which are completely encapsulated by a varying number of curved graphite layers, by varying the composition of the target Co-Ni alloys in the evaporation process. In this way, not only the magnetic properties can be varied but also the dielectric properties of the magnetic nanocapsules can be optimized in order to improve the impedance match, to broaden the EMW absorption bandwidth and to enhance the absorption.

## Experimental

$\text{Co}_x\text{Ni}_{100-x}$ /graphite layers nanocapsules were in-situ synthesized by high-temperature arc-plasma evaporation.<sup>32-35</sup> Alloy ingots are used as the anodes and a graphite rod with

8 mm diameter as the cathode. The anode and cathode are placed in a water-cooled graphite crucible and a holder, respectively, and kept at 2-3 mm distance. The plasma arc is maintained for 1 hr. Then, the residual gas is pumped out and the black powder, which has formed on the inner surface of the water-cooled cover of the chamber, is collected.

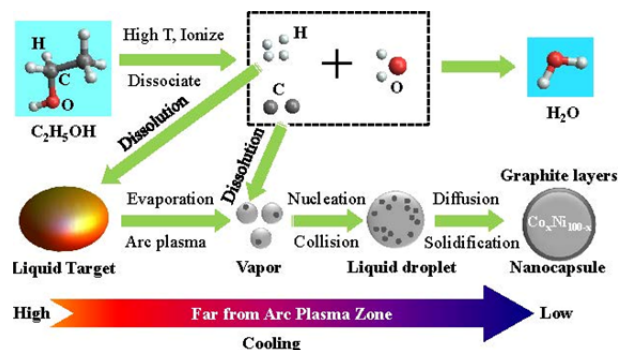


**Fig. 1** Schematic representation of the preparation of magnetic nanoparticles coated with curved graphite layers. At high temperatures, carbon atoms from dissociated ethanol and evaporated metal atoms collide with each other and form aggregates in the arc plasma zone. At low temperature, these aggregates condense due to collision to liquid droplets which are supersaturated of carbon. Further cooling leads to carbon atoms diffusing out of the particles. As a result, the carbon atoms form graphite layers.

The crystal structure of the cores and shells of the nanocapsules were characterized by x-ray diffraction (XRD) with  $\text{Cu-K}\alpha$  radiation (wave length = 0.154056 nm). The composition and size distribution of the particles were analyzed by scanning electron microscopy (SEM, Inspect F50). The microstructure and morphology were investigated in detail by high-resolution transmission electron microscopy (HRTEM, FEI Tecnai F20) with an emission voltage of 200 kV. The magnetic properties were measured in a superconducting quantum interference device (SQUID, Quantum Design MPMS-7). The 40 wt.% of the as-prepared nanocapsules and 60 wt.% of liquid paraffin were uniformly mixed with hexane by ultrasonic waves. Then, the hexane was evaporated and the composites were pressed into a toroid (outer diameter  $\times$  inner diameter  $\times$  thickness = 7.00 mm  $\times$  3.00 mm  $\times$  2.00 mm) for measurement of the EMW absorption. After the (Short, Open, Load, Thru) calibration process was performed, the EM properties of the composites were measured from 2 to 18 GHz by means of an Agilent 8722ES vector network analyzer. The complex relative permittivity and permeability are obtained from the scattering parameters. Using the measured EM parameters, the reflection loss (RL) is derived by means of transmission-line theory, which is widely used to evaluate the microwave absorption of materials.<sup>14, 17, 22, 36</sup>

## Preparation and characterization

The preparation process and formation mechanism of  $\text{Co}_x\text{Ni}_{100-x}$  coated with curved graphite layers are depicted in Fig. 1. After evacuating the chamber ( $3.0 \times 10^{-3}$  Pa), the chamber is filled with a 5:1 Ar/ $\text{H}_2$  gas mixture as a plasma gas with a pressure of 0.022 MPa. 30 ml ethanol ( $\text{C}_2\text{H}_5\text{OH}$ ) is injected into the chamber as carbon source. Then, a plasma arc of the Ar/ $\text{H}_2$  mixture is triggered by applying a voltage of 20 V.  $\text{Co}_x\text{Ni}_{100-x}$  alloy ingots with  $x = 20, 40, 60$  and  $80$  (30 g weight, 2–3 cm diameter and 99.8 wt.% purity), prepared by arc-melting under a high-purity argon, were used as anode material. At very high temperature, the anode melts and metal atoms or clusters evaporate. The targets form an ellipsoidal molten pool in a bowl-like graphite crucible due to the low wettability between the liquid metal and the crucible with its smooth surface, which is different from the flat-bottomed crucible in earlier reported arc-melting method.<sup>37</sup> In the plasma, at high temperature and plasma, the ethanol vapour dissociates into atomic C, H and O. The H atoms dissolve into the liquid targets, which promotes evaporation of the metal atoms.<sup>38</sup> Because of the small interface between the targets and the graphite crucible, most of the carbon comes from the ethanol and not from the crucible, and is concentrated in the discharge zone and not in the melt.<sup>31</sup> Therefore, the vaporized carbon and evaporated metal atoms collide with each other and form aggregates in the arc plasma zone. These aggregates are swept out of the plasma zone by the arc pressure. Colliding aggregates begin to nucleate and condense to supersaturated droplets of carbon. When droplets are far from arc zone with the help of the gas circumfluence, upon cooling, carbon atoms separate out of droplets and form curved graphite layers at the surface. In order to obtain larger nanoparticles and to make more carbon atoms migrate to the surface than other nanocapsules, no cold blowing gas was used in our experiment.<sup>4, 37</sup> In this way, by means of metal catalysis, the carbon atoms form curved graphite layers at the spherical surface of the metallic core, just like the synthesis of graphite at the surface of nickel substrate by the segregation technique.<sup>26, 27</sup>

The XRD patterns of the  $\text{Co}_x\text{Ni}_{100-x}$  nanocapsules (samples S1–S4) are shown in Fig. 2. All sharp reflections can be assigned to the face-centered-cubic (FCC) CoNi solid solution. Under Ar/ $\text{H}_2$  mixture, no graphite impurity and oxides are detected, which indicates that the CoNi cores are not oxidized by air. With increasing cobalt content, the (111) reflection shifts to lower angles and the lattice parameter increases from 0.20386 nm to 0.20456 nm due to the larger atomic radius of cobalt and doped carbon atoms. EDX (energy dispersive X-ray spectroscopy) and XPS (X-ray photoelectron spectroscopy) with the depth larger than 10 nm analyses confirm the composition of the  $\text{Co}_x\text{Ni}_{100-x}$  nanocapsules. In Table I, it can be seen that the compositions of the as-prepared nanocapsules are very similar to the master alloys. The small difference is attributed to the

different vapour pressures and melting points of cobalt and nickel. Above results demonstrate that single-phase  $\text{Co}_x\text{Ni}_{100-x}$  cores with controllable composition can be obtained via the modulation of the master-alloy composition. The as-prepared samples display spherical nanoparticles with similar size distribution as shown in SEM images (Figs. S1).

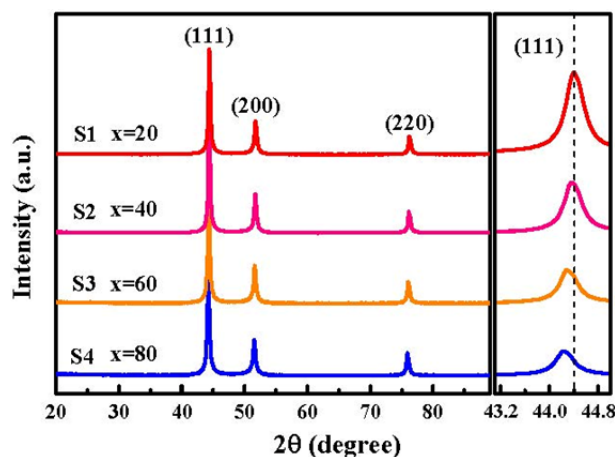


**Fig. 2** XRD patterns of the samples S1, S2, S3 and S4. The right-hand panel shows an enlarged image of the (111) reflection.

To investigate the microstructure and morphology of the  $\text{Co}_x\text{Ni}_{100-x}$  nanocapsules, TEM and HRTEM studies have been made. A representative overview of the TEM images in Figs. 3(a–d) confirms the spherical shape of the nanoparticles with some irregular spheres. The measured size of the nanocapsules ranges from 40 to 110 nm for all samples, which is consistent with the results of SEM. The detailed microstructures of the graphite layers and the metal cores of the nanocapsules are shown in the HRTEM images (Figs. 3(e–h)). One can see that all samples have the core/shell structure. The clear atomic planes with a distance of 0.34 nm (in the [0001] direction) shown in the inset of Fig. 3(f), confirms that curved graphite layers coat the surface of the  $\text{Co}_x\text{Ni}_{100-x}$  cores. Interestingly, one can clearly observe that the number of graphite layers gradually increases from 3–4 layers for S1, 10–12 layers for S2 to 20–30 layers for S3, respectively, and then decreases to 7–8 layers for S4. The HRTEM results show that the number of graphite layers can be successfully controlled by modulating the composition of the metal core, which can also be extended to other core/shell structures. With the increase from 20 at.% to 40 at.% of Co atom in  $\text{Co}_x\text{Ni}_{100-x}$  core for S1 to S2, the increased number of graphite layers is attributed to the improved catalytic growth of carbon of the magnetic core in S2. With further increasing Co content, the catalytic activity of the magnetic core reaches a maximum for S3. Further addition of Co atom for S4 decreases the activity of the core for the growth of graphite layers. The inset of Fig. 3(h) shows a plane spacing of 0.20 nm in the [111] direction of the CoNi nanocrystal and the Fast Fourier Transform (FFT) pattern.

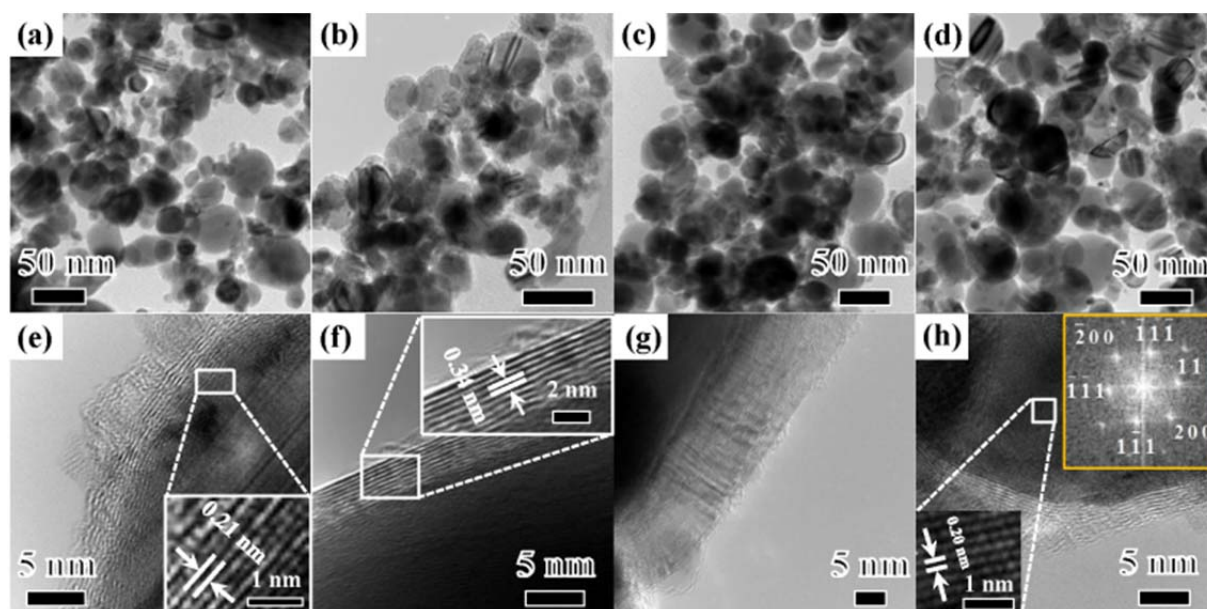


**Fig. 3** (a-d) TEM images and (e-h) high-resolution-TEM images of the samples S1 S2, S3 and S4, respectively. The inset of (e) shows the mixed region of metal nanoparticles and graphite layers. The inset of (f) shows curved graphite layers and the insets of (h) the lattice planes and an FFT image of the metal core.

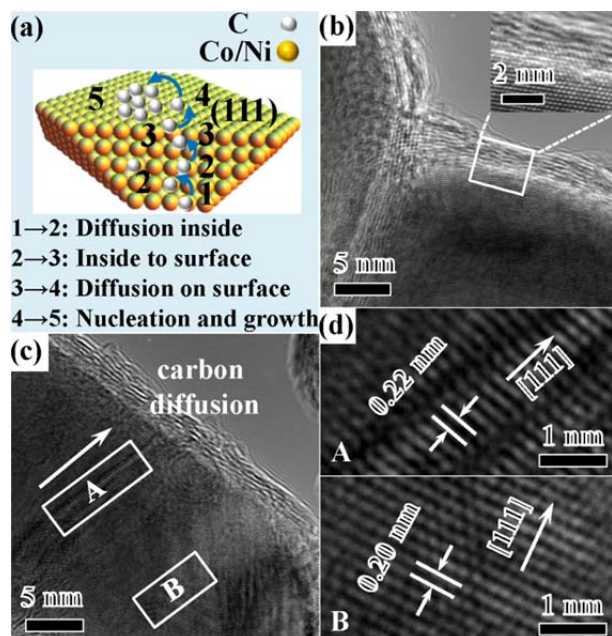


**Fig. 4** (a) Sketch of a possible diffusion path of carbon atoms; (b) Interface between metal core and graphite layers; (c) Diffusion path of carbon atoms in the metal core; (d) Enlarged image of the two regions (A and B) in (c).

To illustrate the growth mechanism of the  $\text{Co}_x\text{Ni}_{100-x}$ /graphite layers nanocapsules, HRTEM images of different regions of samples are shown in Fig. 4. A sketch of a possible diffusion path of carbon along the [111] direction is shown in Fig. 4(a). A clear interface between the metal cores and the graphite layers is observed in Fig. 4(b). In this transition region of metal cores and graphite layers the lattice distance between the (111) planes is 0.21 nm (see Figs. 3(e) and 4(b)), and which is slightly larger than that the distance inside the metal core. When the carbon atoms cannot diffuse from the inside to the surface of the metal cores, they will occupy interstitial sites in CoNi and which will give rise to expansion of the lattice. In Fig. 4(c), two different regions can be distinguished of which an enlarged image is shown in Fig. 4(d). The (111) plane distance in region A is about 0.22 nm and is larger than in region B. The increased distance of the (111) planes shows that the carbon atoms mostly diffuse via the (111) planes of CoNi, which is the same diffusion path as in the formation of graphene on the metal substrate.<sup>26</sup>

## Results and discussion

TEM images show the local information for the carbon shell thickness of nanocapsules. To investigate the average shell thickness of the nanocapsules, thermal gravimetric analysis (TGA) and differential scanning calorimetry (DSC) were

conducted under 30 ml/min air flow from 100 °C to 700 °C with a heating rate of 10 °C/min. The results of the samples S1, S2, S3 and S4 are shown in Fig. 5 (a-d). Generally, thicker shell enhances the anti-oxidative ability more in the same environment and at the same temperature-change rate. The two prominent DSC peaks of sample S3, as compared with sample S1, shift about 20 to 30 °C to higher temperatures, which indicates that the average carbon shell is thicker in S3.<sup>10, 14, 15</sup> However, for samples S2 and S4, the positions of DSC peaks are almost same with each other, which consists with TEM and permittivity results.

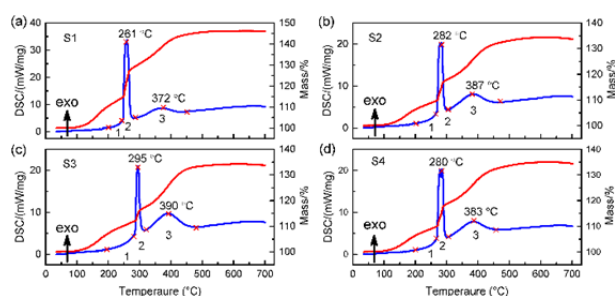


**Fig. 5** DSC (blue line) and TGA (red line) curves of the samples S1, S2, S3 and S4.

The magnetic hysteresis loops of  $\text{Co}_x\text{Ni}_{100-x}$  nanocapsules at 295 K are shown in Fig. 6. As shown in the inset of Fig. 6, from S1 to S4, the saturation magnetization ( $M_s$ ) increases from 64 to 110 emu/g and the coercive force ( $H_c$ ) increases from 125 to 316 Oe. The increase of  $M_s$  with increasing cobalt is due to the larger atomic magnetic moment than nickel. The data are listed in Table I. Comparing with the theoretical value of bulk CoNi alloys, the saturated magnetization of CoNi/C nanocapsules decreases about 20 %. Generally, the magnetic properties of

nanomaterials strongly depend on the quality of magnetic materials, the size and shape of nanoparticles and even preparation method. In the nanocapsule of  $\text{Co}_x\text{Ni}_{100-x}/\text{graphite}$ , there is no amorphous carbon, since ethanol was used as carbon source during the preparation. The carbon mass content in the nanocapsule measured through DSC and TGA is lower than 10 wt. %, as shown in Table SI. Therefore, the decrease of  $M_s$  cannot be completely attributed to the existence of nonmagnetic carbon, which is also related to the doped non-magnetic carbon atoms in the CoNi lattice and the size distribution and shape of nanocapsules. We compare our experimental results in this work to the previous results in literatures, as shown in Fig. S2. The magnetization corresponding to different composition of CoNi nanomaterials displays wide range. Our results are well fit the magnetization range under different Co content.

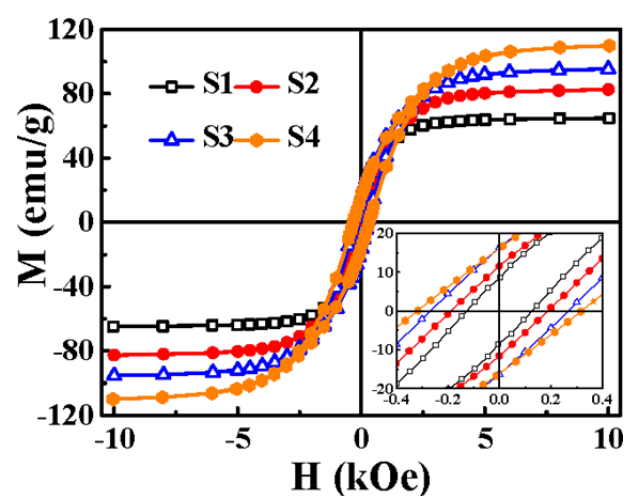


**Fig. 6** Magnetic hysteresis loops at 295 K of the samples S1, S2, S3 and S4 at 295 K. The inset shows an enlarged image.

**Table I** Co content of the master alloys and of  $\text{Co}_x\text{Ni}_{100-x}$  nanocapsules (samples S1, S2, S3 and S4); Lattice distance ( $L$ ) of (111) planes, saturation magnetization ( $M_s$ ), coercive force ( $H_c$ ) and frequency ( $f_m$ ) position.

Samples	Master (at. % Co)	Nanocapsules (at. % Co)	$L$ (nm)	$M_s$ (emu/g)	$H_c$ (Oe)	$f_m$ (GHz)
S1	20	19	0.20386	64	125	9.5
S2	40	38	0.20402	82	181	12.1
S3	60	59	0.20437	95	268	15.1
S4	80	79	0.20456	110	316	15.3

The frequency dependence of the relative complex permittivity and permeability in the 2-18 GHz range are shown in Fig. 7 for the four samples. As can be seen in Figs. 7 (a) and (b), the real part ( $\epsilon'$ ) and the imaginary part ( $\epsilon''$ ) of the permittivity of all samples display a similar tendency of

decreasing with increasing frequency in the whole frequency range. This is attributed to the delayed response of the dipole-polarization to the electric-field change at higher frequencies.<sup>39</sup> Due to charge transfer between the metal and carbon, electric dipoles can be formed at the interface of the

Co<sub>x</sub>Ni<sub>100-x</sub> core and the graphite layers which will produce interface polarization under the EMW excitation. In addition, the many defects in the metal cores and the strongly curved graphite layers as shown in the HRTEM images, will also produce electric dipoles, which leads to other types of polarization loss in different frequency ranges.<sup>5, 10, 14</sup> For all four samples, two weak resonance peaks around 9 GHz and 14 GHz are observed, which are attributed to above mentioned electric dipoles. Both  $\epsilon'$  and  $\epsilon''$  gradually increase with increasing cobalt content from S1 to S3. However, for S4, when the cobalt content reaches 80 at.%, both  $\epsilon'$  and  $\epsilon''$  are smaller than for S2 and S3, but still larger than for S1. This variation of the permittivity is associated with the variation of the number of graphite layers of the nanocapsules as has been seen in HRTEM and DSC results.

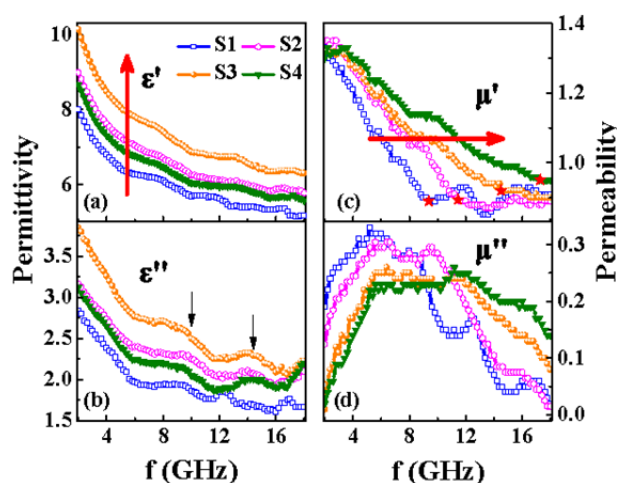


**Fig. 7** Frequency dependence of (a) and (b) the relative complex permittivity and (c) and (d) the relative complex permeability of S1, S2, S3 and S4 dispersed in paraffin with 40 wt.% nanocapsules.

The frequency dependencies of the real part ( $\mu'$ ) and the imaginary part ( $\mu''$ ) of the relative complex permeability  $\mu_r$  are presented in Figs. 7(c) and (d). For all samples,  $\mu'$  initially decreases almost monotonously with increasing frequency. Above a certain frequency, being 9.4 GHz, 11.5 GHz, 14.5 GHz and 17.1 GHz for S1, S2, S3 and S4, respectively, the value of  $\mu'$  is almost constant. On the other hand, for all samples  $\mu''$  exhibits a very broad resonance peak in different frequency ranges, which corresponds to multiple magnetic resonances (MMR).<sup>4, 40</sup> For S1 to S4, the frequency ranges of the broad peak are 5.2–8.7 GHz, 5.9–15.9 GHz, 5.6–9.8 GHz and 5.8–11.9 GHz, respectively. The clear blue-shift of the frequency where  $\mu'$  becomes constant and of the

resonance peaks should be attributed to the magneto-crystalline anisotropy of the Co<sub>x</sub>Ni<sub>100-x</sub> cores which increases from S1 to S4, as is illustrated by the increasing  $H_c$  values listed in Table I. In general, the EMW magnetic loss of nanoparticles mainly results from various kinds of magnetic resonances, from hysteresis and eddy-currents.<sup>6</sup> For the present Co<sub>x</sub>Ni<sub>100-x</sub> nanocapsules, the magnetic loss is mostly attributed to magnetic resonances including natural resonance and exchange resonance.<sup>4, 7, 10</sup> Because of the rapid evaporation at high temperature and the absence of a cold blowing gas, as used in the preparation of other core/shell structures,<sup>4, 37</sup> the Co<sub>x</sub>Ni<sub>100-x</sub> nanocapsules have a broader size distribution and a larger average diameter, which is beneficial to broadening of the absorption band width. For all four samples, the dielectric loss of the samples is all larger than the magnetic loss (Fig. S3).

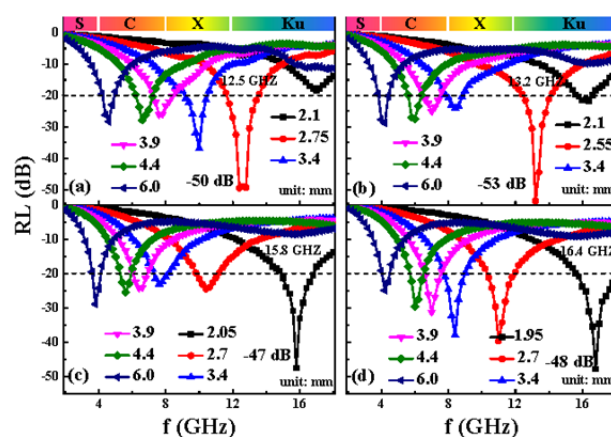


**Fig. 8** Frequency dependence of the microwave RL of the samples S1, S2, S3 and S4 shown in (a), (b), (c) and (d), respectively.

The frequency dependence of the RL of all composites consisting of 40 wt.% nanocapsules and 60 wt.% paraffin with varying thickness on the EMW frequency in 2–18 GHz is presented in Fig. 8. All nanocapsules exhibit broadband microwave absorption. The width of the absorption band with RL exceeding  $-20$  dB (99 % absorption) is 9.3 GHz (4.0–13.6), 12.9 GHz (3.8–16.6), 13.5 GHz (3.4–16.9) and 14 GHz (3.8–18) for S1, S2, S3 and S4 by varying the absorber thickness, respectively. The maximal RL value reaches  $-50$  dB at 12.5 GHz for S1 with thickness of 2.75 mm,  $-53$  dB at 13.2 GHz with thickness of 2.55 mm for S2,  $-47$  dB at 15.8 GHz with thickness of 2.05 mm for S3 and  $-48$  dB at 16.4 GHz with thickness of 1.95 mm for S4. The maximal RL shifts from low to high frequency, which is attributed to the shift of the

matching range of magnetic and dielectric loss from S1 to S4. In Table II, the absorbing performance of the present  $\text{Co}_x\text{Ni}_{100-x}$  nanocapsules is compared with other nanocomposite systems reported recently.<sup>6, 18-21, 41</sup> It can be seen that the CoNi nanocapsules have stronger RL absorption and broader bandwidth at a lower mass density and for smaller absorber thickness. To further display the dependence of RL on the thickness of the absorber and the microwave frequency, a three dimensional (3D) and a contour map are shown for S2 in Figs. 9(a) and (b). It is seen that the  $\text{Co}_{40}\text{Ni}_{60}$  nanocapsules have an outstanding performance (RL < -20 dB) in the whole 2-18 GHz range for different absorber thicknesses. The most important result is that the absorption bandwidth of a single absorber is large, which is clearly seen in Fig. 9(b). For an absorber thickness of 2.55 mm, the absorption band width of  $\text{Co}_{40}\text{Ni}_{60}$  nanocapsules is about 6.4 GHz (9.64-16.03 GHz) with RL values exceeding -10 dB, which almost covers the whole X band and Ku band. This extraordinary absorption of  $\text{Co}_{40}\text{Ni}_{60}$  can be attributed to enhanced dielectric loss and proper EM match by simultaneously tuning of the magnetic properties and the number of graphite layers. The optimal thickness ( $d_m$ ) and frequency ( $f_m$ ) of the 3D RL surfaces are marked in Fig. 9(b) by red points. The solid blue line represents the values

calculated with the formula  $d = \lambda/4$ , where  $\lambda = c/(f|\epsilon_r\mu_r|)$  is the wavelength in the composites and  $c$  is the velocity of light in vacuum. The calculated values agree well with the experimental results, which confirms that the Quarter-wavelength model appropriately describes the relationship between the optimal thickness and the frequency of  $\text{Co}_x\text{Ni}_{100-x}$  nanocapsules.<sup>42, 43</sup>

## Conclusions

Nanocapsules consisting of  $\text{Co}_x\text{Ni}_{100-x}$  nanoparticles completely encapsulated by different number of curved graphite layers have been prepared by high-temperature arc-plasma evaporation. By tuning the cobalt content of the alloys, the magnetic and dielectric properties of the nanocapsules can be simultaneously optimized, and the EM match improved. For the  $\text{Co}_{40}\text{Ni}_{60}$  nanocapsules an optimal RL value of -53 dB at 13.2 GHz has been achieved and an absorption bandwidth of 6.4 GHz which almost covers the whole X band and Ku band. The method applied in the present work is very effective for enhancing the EMW absorption by magnetic nanoparticles in the whole 2–18 GHz band and can be extended to other core/shell.

**Table II** Reported microwave-absorption of some nanocomposites. The weight fraction (wt.%) presents the fraction of nanocomposites in the absorber. The absorber thickness denotes the layer-thickness (range) for which RL < -20 dB. The optimal RL value means the largest absolute value of RL, i.e. optimal absorption. The absorption band width is the frequency range in which RL < -20 dB can be achieved.

Samples	Weight fraction (wt. %)	Absorber thickness (mm)	Optimal RL value (dB)	Absorption band width (GHz)	Ref.
Ni/NiO	50	--	-14.9	--	6
Co/C-tubes	30	~2.5-5	-40	~4-10	18
$\alpha$ -Co/graphene	60	2-5	-47.5	3.5-13.5	19
<i>h</i> -Ni/graphene	60	--	-17.8	--	20
Ni/SiO <sub>2</sub>	50	3.9-5.2	-25	5-8	22
LiNiZn ferrite	30	30	-26	3.8-4.3	41
S1	40	2.1-6.0	-50	4.0-13.6	This work
S2	40	2.1-6.0	-53	3.8-16.6	This work
S3	40	2.05-6.0	-47	3.4-16.9	This work
S4	40	1.95-6.0	-48	3.8-18	This work

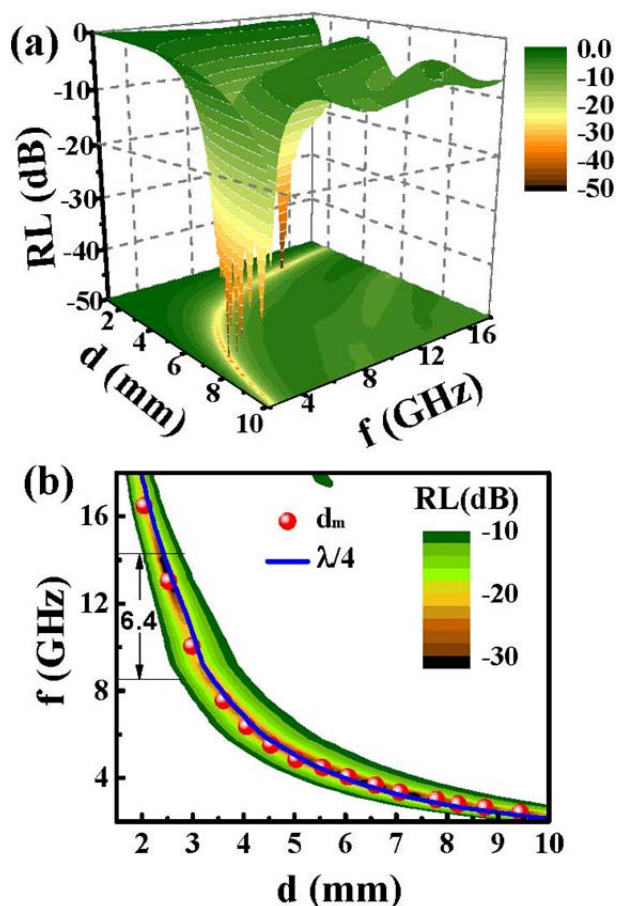


**Fig. 9** (a) Three-dimensional representation and (b) Two dimensional representation of RL for the sample S2; The red points represent frequency and thickness value of maximal RL and blue line represents  $d = \lambda/4$ .

### Acknowledgements

This work was supported by the National Natural Science Foundation of China under Grant number 51271178, 51171185 and the National Basic Research Program No.2012CB933103) of China, Ministry of Science and Technology China.

### Notes and references

- 1 M. T. Sebastian, Dielectric materials for wireless communication, Elsevier, 2010.
- 2 S. Aalto, C. Haarala, A. Bruck, H. Sipila, H. Hamalainen and J. O. Rinne, *J. CEREBR. B.*, 2006, **26**, 885-890.

- 3 S. J. Yan, S. L. Dai, H. Y. Ding, Z. Y. Wang and D. B. Liu, *J. Magn. Magn. Mater.*, 2014, **358–359**, 170-176.
- 4 H. Wang, Y. Dai, W. Gong, D. Geng, S. Ma, D. Li, W. Liu and Z. Zhang, *Appl. Phys. Lett.*, 2013, **102**, 223113-223114.
- 5 P. C. P. Watts, W. K. Hsu, A. Barnes and B. Chambers, *Adv. Mater.*, 2003, **15**, 600-603.
- 6 B. Lu, X. Dong, H. Huang, X. Zhang, X. Zhu, J. Lei and J. Sun, *J. Magn. Magn. Mater.*, 2008, **320**, 1106-1111.
- 7 P. Toneguzzo, G. Viau, O. Acher, F. Fievet-Vincent and F. Fievet, *Adv. Mater.*, 1998, **10**, 1032-1035.
- 8 X.-W. Wei, X.-M. Zhou, K.-L. Wu and Y. Chen, *CrystEngComm*, 2011, **13**, 1328-1332.
- 9 V. B.regar, *IEEE Trans. Magn.*, 2004, **40**, 1679-1684.
- 10 H. Wang, H. Guo, Y. Dai, D. Geng, Z. Han, D. Li, T. Yang, S. Ma, W. Liu and Z. Zhang, *Appl. Phys. Lett.*, 2012, **101**, 083116-083114.
- 11 N. Li, C. W. Hu and M. H. Cao, *Phys. Chem. Chem. Phys.*, 2013, **15**, 7685-7689.
- 12 L. Yan, J. Wang, X. Han, Y. Ren, Q. Liu and F. Li, *Nanotechnology*, 2010, **21**, 095708.
- 13 S.-W. Choi, J. Y. Park and S. S. Kim, *Nanotechnology*, 2009, **20**, 465603.
- 14 X. Zhang, X. Dong, H. Huang, D. Wang, B. Lv and J. Lei, *Nanotechnology*, 2007, **18**, 275701.
- 15 R. C. Che, L. M. Peng, X. F. Duan, Q. Chen and X. L. Liang, *Adv. Mater.*, 2004, **16**, 401-405.
- 16 F. Wen, F. Zhang and Z. Liu, *J. Phys. Chem. C*, 2011, **115**, 14025-14030.
- 17 Y. Fan, H. Yang, X. Liu, H. Zhu and G. Zou, *J. Alloys. Compd.*, 2008, **461**, 490-494.
- 18 Q. Liu, D. Zhang and T. Fan, *Appl. Phys. Lett.*, 2008, **93**, 013110-013113.
- 19 G. Pan, J. Zhu, S. Ma, G. Sun and X. Yang, *ACS Appl. Mater. Interfaces*, 2013, **5**, 12716-12724.
- 20 T. Chen, F. Deng, J. Zhu, C. Chen, G. Sun, S. Ma and X. Yang, *J. Mater. Chem.*, 2012, **22**, 15190-15197.
- 21 Z. Han, D. Li, H. Wang, X. G. Liu, J. Li, D. Y. Geng, and Z. D. Zhang, *Appl. Phys. Lett.*, 2009, **95**, 023114.
- 22 X. Zhang, H. Huang and X. Dong, *J. Phys. Chem. C*, 2013, **117**, 8563-8569.
- 23 X.C. Gui, K.L. Wang, A.Y. Cao, J.Q. Wei, R.T. Lv, F.Y. Kang, Q.K. Shu, Y. Jia, and D.H. Wu, *J. Nanosci. Nanotech.*, 2010, **10**, 1-6.
- 24 X. F. Zhang, X.L. Dong, H. Huang, B. Lv, J.P. Lei and C.J. Choi, *J. Phys. D: Appl. Phys.*, 2007, **40**, 5383-5387.
- 25 X. L. Dong, Z. D. Zhang, Y. C. Chuang, and S. R., Jin, *PHYS. REV. B*, 1999, **60**, 3017-3020.
- 26 N. Liu, L. Fu, B. Dai, K. Yan, X. Liu, R. Zhao, Y. Zhang and Z. Liu, *Nano Lett.*, 2010, **11**, 297-303.
- 27 Z. Peng, Z. Yan, Z. Sun and J. M. Tour, *Acs Nano*, 2011, **5**, 8241-8247.
- 28 B. S. Berry, *J. Appl. Phys.*, 1973, **44**, 3792-3793.
- 29 R. B. McLellan, C. Ko and M. L. Wasz, *J. Phys. Chem. Solids*, 1992, **53**, 1269-1273.
- 30 M. Yudasaka, R. Yamada, N. Sensui, T. Wilkins, T. Ichihashi and S. Iijima, *J. Phys. Chem. B*, 1999, **103**, 6224-6229.

- 31 L. Tan, M. Zeng, T. Zhang and L. Fu, *Nanoscale*, 2015, **7**, 9105-9121.
- 32 A. Bianco, H.-M. Cheng, T. Enoki, Y. Gogotsi, R. H. Hurt, N. Koratkar, T. Kyotani, M. Monthieux, C. R. Park, J. M. D. Tascon and J. Zhang, *Carbon*, 2013, **65**, 1-6.
- 33 S. K. Sengar, B. R. Mehta, R. Kumar and V. Singh, *Sci Rep.*, 2013, **3**, 2814.
- 34 D. Matsuura and T. Kizuka, *J. Nanomater.*, 2012, **2012**, 1-7.
- 35 A. Dahal and M. Batzill, *Nanoscale*, 2014, **6**, 2548-2562.
- 36 Y. Naito and K. Suetake, *IEEE Trans. Microw. Theory Techn.*, 1971, **19**, 65-72.
- 37 J. J. Host, V. P. Dravid and M.-H. Teng, *J. Mater. Res.*, 1998, **13**, 2547-2555.
- 38 J. Li, S. Ma, H. Wang, W. Gong, J. Jiang, S. Li, Y. Wang, D. Geng and Z. Zhang, *J. Mat. Sci. T.*, 2014, **30**, 973-978.
- 39 K. C. Kao, *Dielectric phenomena in solids*, Academic press, 2004.
- 40 J. Ma, J. Li, X. Ni, X. Zhang and J. Huang, *Appl. Phys. Lett.*, 2009, **95**, 102503-102505.
- 41 A. N. Yusoff, M. H. Abdullah, S. H. Ahmad, S. F. Jusoh, A. A. Mansor and S. A. A. Hamid, *J. Appl. Phys.*, 2002, **92**, 876-882.
- 42 T. Inui, K. Konishi and K. Oda, *IEEE Trans. Magn.*, 1999, **35**, 3148-3150.
- 43 B. Wang, J. Wei, Y. Yang, T. Wang and F. Li, *J. Magn. Mater.*, 2011, **323**, 1101-1103.